

Contents lists available at ScienceDirect

International Journal of Plasticity

journal homepage: www.elsevier.com/locate/ijplas



A continuum dislocation-based model of wedge microindentation of single crystals



Giacomo Po*, Yue Huang, Nasr Ghoniem

Department of Mechanical and Aerospace Engineering, University of California Los Angeles, Los Angeles, CA, 90095, USA

ARTICLE INFO

Keywords:
Dislocation density tensor
Finite deformation
Indentation
Dislocation patterns

ABSTRACT

Recent Electron Backscatter Diffraction (EBSD) experiments have revealed the emergence of heterogeneous dislocation microstructures forming under a wedge indenter in fcc crystals, where micro-meter dislocation patterns challenge the predictions of traditional models of plasticity. In order to explain the formation of these features and develop a relationship between the forcedisplacement curve and the dislocation substructure, we present here a model of wedge indentation based on the continuum theory of dislocations. The model accounts for large deformation kinematics through the multiplicative split of the deformation gradient tensor, where the incompatible plastic component of deformation results from the flux of dislocations on different and interacting slips systems. Constitutive equations for dislocation fluxes are determined from a dissipative variational principle. As a result, each dislocation density satisfies an initialboundary value problem with convective-diffusive character, which is coupled to the macroscopic stress and displacement fields governing the deformation process. Solution to the selfconsistent continuum formulation is found using the finite element method. Computer simulations mimic the experimental conditions of wedge micro-indentation experiments into Ni singlecrystals used by Kysar et al. (2010a). A comparison of overall dislocation density distribution and macroscopic mechanical response shows good overall agreement with the experimental results in terms of the detailed features of dislocation patterns and lattice rotations as well as the macroscopic force-displacement response.

1. Introduction

Due to its simplicity, the need for minimal sample preparation, and its non-destructive character, indentation is a mechanical test which is routinely used for characterization and quality control of materials. Traditional indentation tests measure the ratio between the applied load and the optically-imaged residual imprint area, a quantity known as *indentation hardness*. In metals, indentation hardness is not only a measure of whether annealing or hardening treatments have been carried out correctly, but also a quantity from which other mechanical properties can be extracted. A notable example of this practice is Tabor's law relating hardness to yield strength (Tabor, 1951). Indentation plays an important role in the mechanical characterization of brittle ceramics, since the hydrostatic component of stress below the indenter tip hinders premature fracture and reveals properties of plastic deformation otherwise inaccessible via uniaxial tests. For example, Knoop hardness anisotropy measurements were instrumental in determining the active slip systems in transition-metal carbides as a function of temperature (Hannink et al., 1972), while the size of indentation cracks was found to relate to the toughness of ceramics (Anstis et al., 1981).

E-mail address: gpo@ucla.edu (G. Po).

^{*} Corresponding author.

Over the past three decades, the interest in understanding the deformation processes of materials in small volumes, such as thin films, multilayer materials, and heterogeneous composites, has attracted renewed attention on indentation because of its ability to probe mechanical properties otherwise inaccessible via other methods. The difficulty of accurately measuring the imprint area at small depths has promoted the development of depth-sensing indentation (also known as instrumented indentation, or simply nanoindentation), a technique where the full history of load vs. depth of penetration (*P* vs. *h*) is measured during the test (Pethicai et al., 1983). The rich amount of information contained in the *P-h* curves, especially when nanoindenters are equipped with the capability of continuous stiffness measurements (CSM), have enabled new ways of probing materials to extract their mechanical properties (Li and Bhushan, 2002; Vanlandingham, 2003; Schuh, 2006; Fischer-Cripps, 2006; Gouldstone et al., 2007). Examples include hardness and elastic moduli (Oliver and Pharr, 1992), residual stresses (Suresh and Giannakopoulos, 1998), fracture toughness of thin films (Li et al., 1997), fatigue strength (Schwaiger and Kraft, 1999), power-low elasto-plastic response and power-low creep response (Cheng and Cheng, 2004).

A remarkable discovery enabled by nanoindentation is that the indentation size effect (ISE) is an intrinsic property of plastic deformation, as opposed to an experimental artifact (Pharr et al., 2010). The intriguing aspect of the ISE is that it belies the traditional understanding of hardness as a constant material property when measured with self-similar indenters (Tabor, 1951; Xue et al., 2002). A widely accepted explanation of the ISE was proposed by Nix and Gao (1998), who interpreted the ISE as a manifestation of geometrically necessary dislocations (GNDs) accumulated under the indenter tip. The prospect of using indentation as a tool to develop a more fundamental understanding of plasticity in terms of structures and mechanics of dislocations has promoted new experimental and computational research. In this line of inquiry, recent high-resolution EBSD studies have revealed the complex morphology of the GND structures forming beneath indenters (Zaafarani et al., 2006; Kysar et al., 2007, 2010a; Rester et al., 2008; Demir et al., 2009; Dahlberg et al., 2014; Ruggles et al., 2016). By offering a direct view of how materials defects collectively respond to inhomogeneous loads, these experiments constitute an important reference for microstructure-based models of plasticity. Theory (Zhang et al., 2007; Xiong et al., 2012; Öztop et al., 2013), Molecular Dynamics (MD) simulations (de la Fuente et al., 2002; Li et al., 2002; Lilleodden et al., 2003; Fang et al., 2003; Nair et al., 2008), and discrete Dislocation Dynamics simulations (Fivel et al., 1997, 1998; Balint et al., 2006; Zhang et al., 2014; Po et al., 2014) have examined the properties of dislocation structures generated by indenters. However, because of limitations in space and time scales, only continuum plasticity simulations have allowed a comparison between modeling results and microstructures revealed by EBSD measurements. In the last decade, a number of continuum models have been proposed to explain the sub-surface fields generated by indenters. These include continuum plasticity (Gan et al., 2008; Saito et al., 2012), crystal plasticity (Lee and Chen, 2010; Sabnis et al., 2013; Zhang et al., 2014), and Kocks-Mecking type models (Zaafarani et al., 2008; Engels et al., 2012). The drawback of these plasticity models, however, is that they rely on phenomenological equations to determine the amount of plastic slip at any given point, and therefore they are not well-suited to understand dislocation structures formation in terms of elementary dislocation mechanics. By contrast, a variety of plasticity frameworks broadly classified here as Continuum Dislocation-based Plasticity methods (CDP), use dislocation density-type state variables, and plastic deformation is self-consistently governed by their transport (Acharya, 2001; Arsenlis et al., 2004; Yefimov et al., 2004; Hochrainer et al., 2014; Xia and El-Azab, 2015). Application of such models to the investigation of dislocation patterns formed under indenters has been limited. Po and Ghoniem (2012) have developed a kinematically-linear CDD model which mimics the wedge-indentation experiment of Kysar et al. (2010a), where the plane-strain deformation process was modeled by six families of effective edge dislocations. Reuber et al. (2014) have considered the same problem within finite deformation settings, but with linearized dislocation density transport equations, a dislocation population comprising both edge and screw dislocations, and without an energetic contribution of the dislocation densities. Baitsch et al. (2015) a single-slip system simulation of the wedge indentation problem in a linearized and non-dissipative framework, where the geometrically-necessary dislocation content results from the minimization on an energy functional first proposed by Berdichevsky (2006).

The objective of this paper is to develop a formulation of continuum dislocation-based plasticity at finite deformation, for applications to the study of dislocation structures which develop under indenters. Our reference experimental condition is the wedge indentation experiment of Kysar et al. (2010a), because it provides a simple pseudo two-dimensional settings. The paper is organized as follows. In section 2 we introduce the finite-strain kinematics of both deformation and dislocation transport within the materials, and seek a thermodynamic closure equation for the dislocation velocity field as a function of internal stress and densities. In section 3, we derive the weak formulation of the three boundary value problems of the model, and solve them for the case of wedge-indentation of a Nickel single crystal as in Kysar et al. (2010a) The aim here is to validate the physically-based model with experiments Kysar et al. (2010a) at the same length scale, and to determine the relationship between the macroscopic force-displacement measurements and the underlying dislocation microstructure. Results and comparison with experiments are provided in terms of load vs displacement curves, lattice rotation, GND density, and dislocation densities on individual slip systems. Discussion and conclusions are finally presented in section 4.

2. Model formulation

The proposed model mimics the experimental conditions of the wedge-indentation experiment of Kysar et al. (2010a). These are illustrated in Fig. 1a, where a face-centered cubic (fcc) single crystal is indented on a (001) plane by a wedge parallel to the [110] direction. As pointed out by Kysar et al. (2005), the line loading induces plane strain deformation in the (110) plane by equally activating pairs of slip systems with identical in-plane components of the Burgers vector, and opposite out-of-plane component. Therefore, the deformation is equivalent to that produced by six *effective* slip systems of *edge* dislocations with slip direction and glide plane normal fully contained in the (110) plane. Slip direction and plane normal of each dislocation family are listed in Table 1c. In

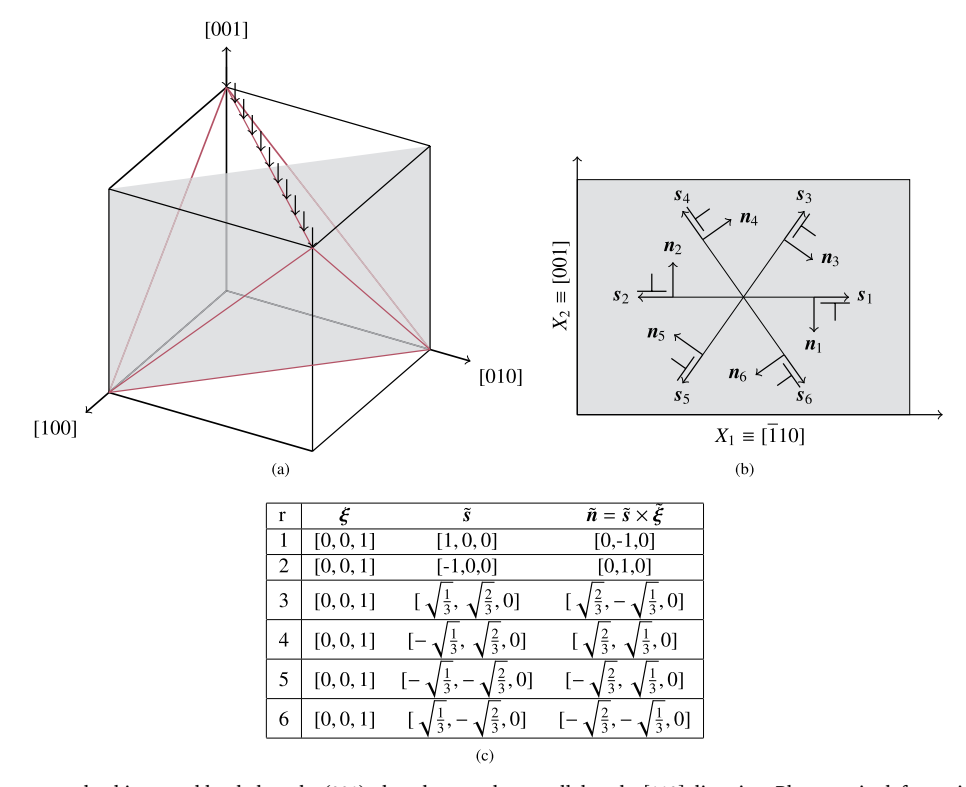


Fig. 1. (a) A face-centered cubic crystal loaded on the (001) plane by a wedge parallel to the [110] direction. Plane strain deformation in obtained on the shaded (110) plane. (b) View of the (110) plane showing the six effective slip systems with edge dislocations densities $g^1(X, t)$, ... $g^6(X, t)$, respectively. (c) Orientation of the effective slip systems in the global reference frame of (b).

the current model, each family is described by a density of dislocations per unit referential area $\varphi^r(X, t)$ (r = 1...6), which is a function of the material coordinate $X = (X_1, X_2)$ in the (110) plane, and time (Fig. 1b). The objective of this section is to formulate a finite-deformation model of the plane-strain indentation process, where the plastic deformation of the crystal is induced by the transport of these dislocations. Because of the significant geometric changes under the indenter, a finite-deformation model is critical to the description of lattice rotations and the corresponding dislocation microstructure.

In all subsequent development we use indicial notation for tensor fields, with lowercase latin indices referring to coordinates in the spatial configuration, latin uppercase indices to the reference configuration, and greek indices to the intermediate configuration. Differential operators and integral theorems are applied following their "right" definition, as opposed to "left" (Malvern, 1969).

2.1. Kinematics

We adopt the kinematics framework originally proposed by Bilby et al. (1957), Kröner (1960), and Lee (1969), where the total deformation gradient F is multiplicatively split into a lattice-preserving and dislocation-mediated plastic part F^p , and an elastic part F^E associated with lattice stretching, that is

$$F_{iJ} := \frac{\partial x_i}{\partial X_I} = F_{i\alpha}^E F_{cJ}^P \ . \tag{1}$$

It is further assumed that both \mathbf{F}^E and \mathbf{F}^P are orientation preserving, i.e. $J^E = \det(\mathbf{F}^E) > 0$ and $J^P = \det(\mathbf{F}^P) > 0$, so that both the inverse elastic distortion tensor $\mathbf{G}^E = (\mathbf{F}^E)^{-1}$ and the inverse plastic distortion tensor $\mathbf{G}^P = (\mathbf{F}^P)^{-1}$ exist. A fundamental aspect of the multiplicative decomposition (1) is that \mathbf{F}^E and \mathbf{F}^P may be individually incompatible, although their product is the total deformation gradient \mathbf{F} , which is a compatible field by definition. As a consequence, a closed oriented material curve \mathscr{C}_0 maps into a closed material curve \mathscr{C}_i in the spatial configuration, while it transforms into an open curve \mathscr{C}_i in the intermediate configuration. In the \mathbf{FS}/RH convention (de Wit, 1960, 1965), the vector measuring the closure failure of \mathscr{C}_i is:

$$\tilde{B}_{\gamma} := \int_{\mathscr{C}} d\tilde{X}_{\gamma} , \qquad (2)$$

where $d\tilde{X}$ is an infinitesimal material vector in the intermediate configuration. This vector can be mapped to either the reference or the current configuration, therefore allowing the following two sets of identities (Steinmann, 1996):

$$\tilde{B}_{\gamma} := \int_{\tilde{\mathscr{C}}} d\tilde{X}_{\gamma} = \begin{cases} \oint_{\mathscr{C}_{0}} F_{\gamma I}^{P} dX_{I} &= -\int_{\mathscr{D}_{0}} \varepsilon_{JKM} F_{\gamma K,M}^{P} dA_{J} &= -\int_{\tilde{\mathscr{F}}} \frac{1}{J^{F}} \varepsilon_{JKM} F_{\gamma K,M}^{P} F_{\chi J}^{P} d\tilde{A}_{\chi} \\ \oint_{\mathscr{C}_{0}} G_{\gamma i}^{E} dx_{i} &= -\int_{\mathscr{F}_{i}} \varepsilon_{jkm} G_{\gamma k,m}^{E} da_{j} &= -\int_{\tilde{\mathscr{F}}} J^{E} \varepsilon_{jkm} G_{\gamma k,m}^{E} G_{\chi i}^{E} d\tilde{A}_{\chi} \end{cases}$$

$$(3)$$

In (3), \mathscr{G}_0 and \mathscr{G}_t are surfaces bounded by the curves \mathscr{G}_0 and \mathscr{G}_t , respectively, while \mathscr{S}_t is the corresponding collection of area elements in the intermediate configuration. Eq. (3) shows that an elementary area element suffers a closure failure $d\tilde{B} = A \cdot dS_0 = a \cdot dS_t = \alpha \cdot d\tilde{S}_t$, which is measured by different tensors depending on whether the area element is taken in the reference (dS_0) , current (dS_t) , or intermediate configuration $(d\tilde{S}_t)$. From Eq. (3) it can be seen that these tensors have components dS_t

$$A_{\gamma J} = -\varepsilon_{JKM} F_{\gamma K,M}^{P} \tag{4a}$$

$$a_{\gamma}:=-\varepsilon_{jkm}G^{E}_{\gamma k,m}$$
 (4b)

$$\alpha_{\gamma\chi} := -\frac{1}{I^P} \varepsilon_{JKM} F_{\gamma K,M}^P F_{\chi J}^P = -J^E \varepsilon_{jkm} G_{\gamma k,m}^E G_{\chi J}^E . \tag{4c}$$

The mechanical significance of these tensors consists in their role as sources of internal stress in the crystal, as better appreciated in the linearized theory of plastic eigendistortions (Mura, 1982). Adopting a material viewpoint, we henceforth choose to work with the tensor A.

The property that the tensor A measures the local closure failure of an area element inspired Nye (1953) to establish the link between its kinematic definition (4a) and the dislocation content in the crystal, therefore enabling the interpretation of A as a dislocation density tensor. In fact, letting the superscript r identify families of dislocations sharing a common Burgers vector \vec{b}^r and line direction ξ^r and having density ϱ^r per unit reference area normal to their line direction, the dislocation density tensor can be expressed as:

$$A_{\gamma J} = \sum_{r} A_{\gamma J}^{r} , \qquad (5)$$

where the dislocation density tensor of the r-th family is defined as

$$A_{\gamma J}^{r} = \wp^{r} \tilde{b}_{\gamma}^{r} \xi_{J}^{r} \,. \tag{6}$$

In the wedge indentation problem at hand, the summation in (5) runs over the six families of edge dislocations with properties listed in Fig. 1c.

The balance law governing the evolution of each A_{VI}^r is derived in Eq. (A.3), and its local form reads

$$\dot{A}_{\gamma J}^{r} = -\varepsilon_{JKM} (L_{\gamma \chi}^{r} F_{\chi K}^{P})_{,M} + p \tilde{b}_{\gamma}^{r} \xi_{J} , \qquad (7)$$

where $L_{\gamma\chi}^r = \tilde{\varsigma}^r \tilde{b}_{\gamma}^r \varepsilon_{\delta\beta\chi} \tilde{w}_{\delta}^r \tilde{\xi}_{\beta}^r$ is the Burgers vector flux of the *r*-th family, with $\tilde{\varsigma}^r$, \tilde{w}^r , $\tilde{\xi}^r$ being the density, the velocity and line direction in the intermediate configuration, respectively. On the other hand, the rates of the dislocation density tensors (4) can be obtained by differentiating its kinematic definition (Acharya, 2001; Cermelli and Gurtin, 2001; Svendsen, 2002; Arsenlis et al., 2004). In particular, the rate of the tensor \boldsymbol{A} is

$$\dot{A}_{\gamma J} = -\varepsilon_{JKM} (\dot{F}_{\gamma K}^{P})_{,M}, \qquad (8)$$

where $L_{\alpha\beta}^{P}$ is the standard plastic velocity gradient defined by the relation

$$\dot{F}_{\gamma K}^{P} = L_{\gamma \gamma}^{P} F_{\gamma K}^{P} . \tag{9}$$

Two important results are obtained by summing Eq. (7) over all families, comparing to Eq. (8), and invoking the arbitrariness of the plastic deformation process. First, that L^P can be expressed as the sum of the individual dislocation flux tensors

$$L_{\gamma\chi}^{P} = \sum_{r} L_{\gamma\chi}^{r} = \sum_{r} \tilde{b}_{\gamma}^{r} \varepsilon_{\chi\beta\mu} \tilde{w}_{\beta}^{r} \tilde{\varepsilon} \tilde{\xi}_{\mu}^{r} . \tag{10}$$

Second, that the sum of the production terms must vanish in tensorial sense, that is

$$\sum_{r} \tilde{b}_{\gamma}^{r} p^{r} \xi_{J}^{r} = 0. \tag{11}$$

We further assume that only dislocation glide motion is allowed. Therefore the dislocation velocity of family r can be written as $\tilde{w}^r = \tilde{w}\tilde{s}^r$, where \tilde{w}^r is a scalar dislocation velocity field, and \tilde{s}^r is the fixed slip direction appearing in Fig. 1c. In turn, the product $\tilde{n}_{\delta}^r = \varepsilon_{\delta \chi \mu} \tilde{s}_{\chi}^r \tilde{s}_{\mu}^r$ defines the component of the glide plane normal for each slip system, and the plastic velocity gradient reduces to the familiar form encountered in CP theories (Roters et al., 2010)

¹ Note that the first equality in Eq. (4c) is the definition of the tensor α , while the second equality represents the condition that the incompatibilities of F^E and F^P must cancel each other in order to guarantee the compatibility of total deformation.

$$L_{\gamma\delta}^{P} = \sum_{r} \dot{\gamma}^{r} \bar{s}_{\gamma}^{r} \tilde{n}_{\delta}^{r} , \qquad (12)$$

where the slip rates are given by Orowan's equation $\dot{\gamma}^r = \tilde{\varphi}^r \tilde{b} \tilde{w}^r$. Moreover, the trace $L_{\gamma\gamma}^P$ vanishes identically and therefore J^P remains constant at all times. Under these conditions, the balance law Eq. (7) admits the scalar counterpart derived in (A.6), which reads

$$\dot{\varphi}^r = -(\tilde{\varphi}^r \tilde{w}^r \tilde{s}_{\chi}^r G_{K\chi}^P)_{K} + p^r . \tag{13}$$

We remark here that the plastic deformation of the indented crystal is governed by Eqs. (9), (12) and (13), which ultimately depend on the velocities w^r and source terms p^r . Closure equations for these quantities are obtained in the following sections.

2.2. Irreversible thermodynamics

Deriving a closure equation for the dislocation velocity w^r requires a brief foray into irreversible thermodynamics. We begin with the balance equations for the internal energy and entropy densities per unit reference volume ϕ and η , respectively. The local forms of the integral balance laws formulated in Appendix B read

$$\dot{\phi} = P_{iK} \nu_{i,K} - Q_{K,K} + h - \sum_{r} (\varphi^r \varphi^r w_K^r)_{,K} + \sum_{r} \varphi^r p^r , \qquad (14)$$

$$\dot{\eta} = -\left(\frac{Q_K}{T}\right)_{,K} + \frac{h}{T} + \gamma - \sum_r \left(\sigma^r \varphi^r w_K^r\right)_{,K} + \sum_r \sigma^r p^r \ . \tag{15}$$

Here P_{iK} is the first Piola stress, v_i the material velocity, Q_K the referential heat flux, h the heat supply, T is the absolute temperature, and γ is the rate of entropy production per unit reference volume, which must be a positive quantity as dictated by the second law of thermodynamics. The non-standard quantities φ^r and σ^r are, respectively, the energy and entropy per unit length of dislocation which the flux $\varphi^r w^r$ and the source term p^r carry into the control volume.

In order to obtain a dissipation equation we follow the standard procedure of multiplying (15) by T and subtracting the result from (14), assuming uniform temperature for simplicity. This results in

$$P_{iK}\dot{F}_{iK} - \dot{\psi} - \eta \dot{T} + \sum_{r} \mu^{r} \left[-(\varrho^{r} w_{K}^{r})_{,K} + p^{r} \right] - \sum_{r} \varrho^{r} w_{K}^{r} \mu_{,K}^{r} = D \ge 0 ,$$
(16)

where $\psi = \phi - T\eta$ is the Helmholtz free energy density, $\mu^r = \varphi^r - T\sigma^r$ are the "chemical potentials" of the dislocation species, and $D = T\gamma$ is the energy rate dissipated into heat by internal processes, such as internal heat fluxes and dislocation motion within the crystal. In order to proceed further, we assume that the free energy is a function of the elastic Green-Lagrangian strain, temperature, and each of the dislocation densities φ^r , that is

$$\psi = \psi(\mathbf{E}^E, T, \mathbf{g}^r) \,. \tag{17}$$

By sake of (17), and taking into account the balance law (13), Eq. (16) is rewritten as

$$\left(P_{lK}F_{\alpha K}^{P} - \frac{\partial \psi}{\partial E_{\alpha \beta}^{E}}F_{l\beta}^{E}\right)\dot{F}_{i\alpha}^{E} - \left(\frac{\partial \psi}{\partial T} + \eta\right)\dot{T} - \sum_{r}\left(\frac{\partial \psi}{\partial \varsigma^{r}} - \mu^{r}\right)\dot{\varsigma}^{r} + P_{lK}F_{i\alpha}^{E}\dot{F}_{\alpha K}^{P} - \sum_{r}\varsigma^{r}w_{K}^{r}\mu_{,K}^{r} = T\gamma \ge 0.$$

$$(18)$$

The terms in parenthesis in (18) are those that must vanish identically when the dissipation D is assumed to be independent of the rates \dot{F}^E , \dot{T} , and $\dot{\varphi}^r$. This assumption is widely accepted for plastically-deformed metals, and it leads to the following constitutive relations

$$P_{mI} = F_{m\alpha}^{E} \frac{\partial \psi}{\partial E_{\alpha\beta}^{E}} G_{I\beta}^{P} \eta = -\frac{\partial \psi}{\partial T} \mu^{r} = \frac{\partial \psi}{\partial \varsigma^{r}} . \tag{19}$$

The surviving portion of the dissipation equation (16) is further manipulated using (9), (12), and the relation $w_K^r = G_{K\chi}^p \tilde{w}_\chi = G_{K\chi}^p \tilde{w}^r \tilde{s}_\chi^r$ to obtain

$$M_{\beta\alpha} \sum_{r} \varsigma^{r} b \tilde{w}^{r} \tilde{s}_{\alpha}^{r} \tilde{n}_{\beta}^{r} - G_{K\chi}^{P} \sum_{r} \varsigma^{r} \tilde{w}^{r} \tilde{s}_{\chi}^{r} \mu_{,K}^{r} = D \ge 0$$

$$(20)$$

where $M_{\beta\alpha} = F_{\beta K}^P P_{lK} F_{l\alpha}^E J^P$ is the Mandel stress. In the spirit of irreversible thermodynamics, we now regard the dislocation velocity as a generalized irreversible flux which causes internal dissipation. Indeed, both theory and MD simulations indicate that for small dislocation velocity compared to the shear wave speed, dislocations experience a dissipative friction force proportional to their velocity (Lothe, 1962; Nabarro, 1967; Bitzek and Gumbsch, 2005; Olmsted et al., 2005). The simplest form of the dissipation consistent with this observation is

² As a consequence of these simplifications, there is no distinction between the dislocation densities per unit intermediate area $\tilde{\epsilon}^r$ and referential area ϵ^r , although we retain the formal difference between the two.

$$D = \frac{B}{2} \sum_{r} \varrho^{r} (\tilde{w}^{r})^{2} , \qquad (21)$$

where *B* is a coefficient with units of [Pa sec]. With this choice, the velocity of each dislocation family can be obtained from (18) via the principle of maximum dissipation rate (PMEP) (Ziegler, 1983; Ziegler and Wehrli, 1987; Collins and Houlsby, 1997). This yields

$$\tilde{w}^r = \frac{b}{B} \left(\tilde{M}_{\delta \gamma} \tilde{s}_{\gamma}^r \tilde{n}_{\delta}^r - \frac{1}{b} \mu_{,N}^r G_{N\gamma}^p \tilde{s}_{\gamma}^r \right). \tag{22}$$

Note that the term $\tau^r = \bar{M}_{\delta\gamma} \tilde{s}_{\gamma}^r \tilde{n}_{\delta}^r$ is the resolved shear stress in the intermediate configuration, while the term $\tilde{\tau}^r = \frac{1}{b} \mu_{,N}^r G_{N\gamma}^P \tilde{s}_{\gamma}^r$ plays the role of a *back stress* proportional to the gradient of the chemical potential.

2.3. Energy of microstructures

We assume that the free energy density used has the form

$$\psi(E^E, T, \varrho^1, ... \varrho^6) = \psi_E(E^E) + \psi_M(\varrho^1, ... \varrho^6),$$
 (23)

where $\psi_{\!\scriptscriptstyle E}$ is the elastic energy density, while $\psi_{\!\scriptscriptstyle M}$ is microstructural energy. The elastic energy density is

$$\psi_E(\mathbf{E}^E) = \frac{1}{2} \mathbb{C}_{\alpha\beta\gamma\delta} E_{\alpha\beta}^E E_{\gamma\delta}^E, \tag{24}$$

where E^E is the Green-Lagrangian elastic strain. For the cubic Ni single crystal considered here, the elastic tensor $C_{\alpha\beta\gamma\delta}$ contains only the three independent constants c_{11} , c_{12} , and c_{44} listed in table 2c. In general, the microstructural free-energy contains both energetic and entropic contributions, although there is no general consensus on its functional form (Groma et al., 2007, 2010; Kooiman et al., 2014, 2015; 2016; Svendsen and Bargmann, 2010; Mesarovic et al., 2010). Berdichevsky (2006) proposed the simple expression³

$$\psi_M(\varsigma^1, \varsigma^2, ...) = \hat{\psi}_M(\varsigma^T(\varsigma^1, \varsigma^2, ...)) = kc_{44} \ln \frac{1}{1 - \varsigma^T/\varsigma^*},\tag{25}$$

where $g^T = \sum g^r$ is the total dislocation density, c_{44} is the shear modulus, k is a dimensionless parameter and g^* is a saturation density. With this choice, the chemical potential is the same for all scalar dislocation densities, and the back stress becomes proportional to the gradient of the total density, in fact

$$\mu^r = \frac{\partial \hat{\psi}}{\partial \varrho^T} \frac{\partial \varrho^T}{\partial \varrho^r} = \frac{J^P k G}{\varrho^* - \varrho^T} \text{and} \mu_{,N}^r = \frac{J^P k G}{(\varrho^* - \varrho^T)^2} \varrho_{,N}^T . \tag{26}$$

2.4. Dislocation sources and mobility

In three-dimensional space, dislocation lines collide with each other and form junctions, screw dislocations cross slip, and curved dislocations increase their length as they bow out. These mechanisms of length multiplication have no rigorous representation in the two-dimensional picture of equivalent straight dislocations adopted in this paper. The source term p^r which accounts for these processes must therefore be modeled phenomenologically. We assume that on each slip system there is a constant density of Frank-Read sources φ_{FR} , which operate with frequency ν_{fr} . Every time a source bows out and closes on itself, it emits a loop which in the two dimensional framework corresponds to a pair of dislocations on opposite slip systems. Therefore, the production term for each slip system is

$$p^r = g_{FR} \nu^r \,. \tag{27}$$

The frequency v^r is the inverse of the time T^r which is needed to grow an embryonic Frank-Read source of length L into a closed loop of radius αL . This is

$$\nu^{r} = \begin{cases} \frac{\left(|\tau^{r}| - \frac{c_{44}b}{L_{1}}\right)b}{\alpha LB} & \text{if } |\tau^{r}| > \mu b/L_{2} \\ 0 & \text{otherwise} \end{cases}$$
(28)

Finally, a similar consideration about three-dimensional forest hardening suggests to consider the following effective mobility

$$B = \begin{cases} B_0 & \text{if } |\tau^r| > \mu b/L_2 \\ \infty & \text{otherwise} \end{cases}$$
(29)

so that dislocations are actually immobilized below a certain stress threshold. In the real three-dimensional condition, both lengths L_1 and L_2 are related to the average dislocation spacing. Since the only indication of such quantity in the two-dimensional representation is the total dislocation density $g^T = \sum_r g^r$, for simplicity we choose $L_1 = L_2 = 1/\sqrt{g^T}$.

³ Alternative simple formulations include models where the microstructural energy depends on the GND density $\varrho^{\text{GND}} = \sqrt{A_{\gamma J} A_{\gamma J}}/b$, or the SSD density $\varrho^{\text{SSD}} = \varrho^T - \varrho^{\text{GND}}$.

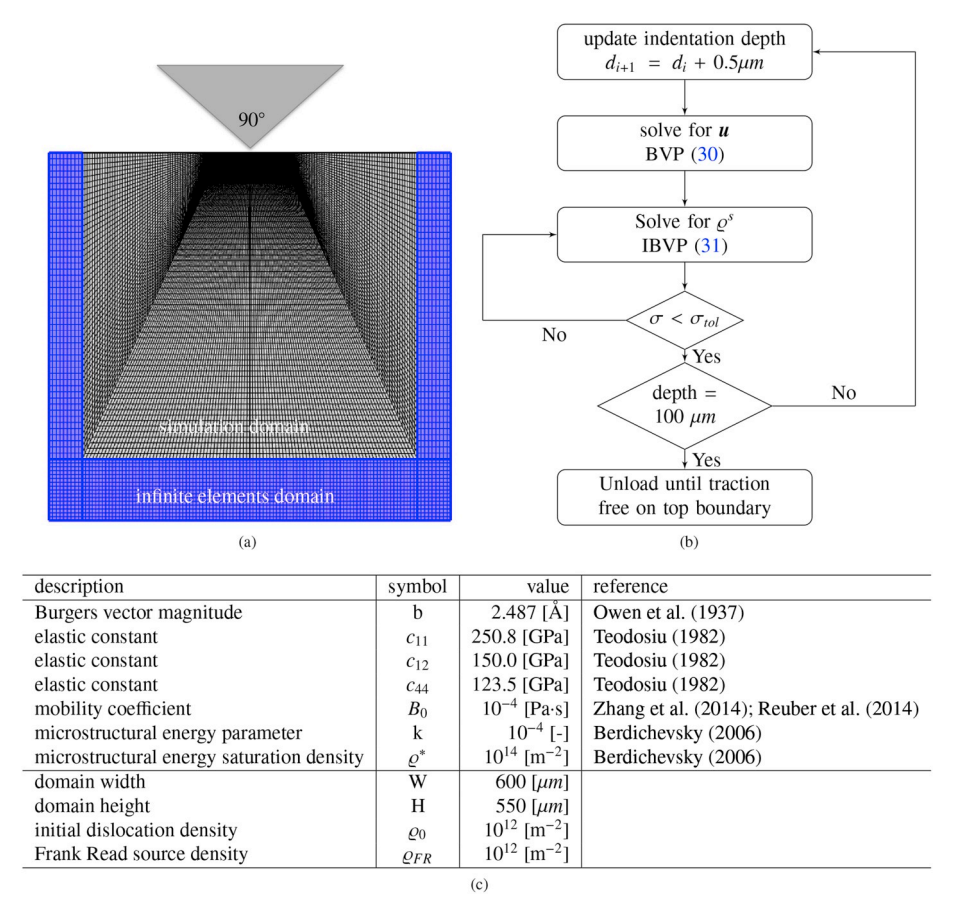


Fig. 2. (a) The simulation domain is a $W \times H$ rectangle surrounded on three sides by infinite elements. Zero traction is prescribed on the lateral boundaries, while zero vertical displacement is prescribed on the bottom boundary. Zero dislocation flux is prescribed on the in-flow portion of the boundary. (b) Staggered solution algorithm for the coupled mechanical and transport problem. (c) Parameters used in the Ni single-crystal model taken from (Owen et al., 1937, Teodosiu, 1982, Zhang et al., 2014, Reuber et al., 2014, Berdichevsky, 2006).

3. Micro-indentation simulations

3.1. Finite element implementation and boundary conditions

The theoretical model developed in the previous sections is implemented numerically using the finite element method (FEM). We consider a single crystal Ni sample oriented as in Fig. 1b. With reference to Fig. 2a, we consider a simulation domain of width $W = 600\mu m$ and height $H = 550\mu m$. A region of infinite elements surrounds this domain on the left, bottom, and right sides. This allows the prescription of boundary conditions on these sides at infinity. In particular, the lateral boundaries of this domain are traction free, while the lower boundary is constrained in the vertical direction. The top surface is indented by a rigid 90° wedge with a tip radius of $R = 10\mu m$. The indenter is pushed into a Ni single crystal in increments of $0.5\mu m$, for a total indentation depth of $100\mu m$. At time t = 0, we assume that each slip system is populate by a uniform density, that is $\varphi^r(X, 0) = \varphi_0 = 10^{12} m^{-2}$ for r = 1...6, so that the GND content o the crystal vanishes identically. We also assume that the crystal is initially plastically undistorted, that is $F^p(X, 0) = I$.

Using these initial conditions, the sequential solution scheme illustrated in Fig. 2b is implemented to find the displacement field \boldsymbol{u} , the plastic distortion field \boldsymbol{F}^p , and the dislocation density fields ς^r (r=1,...6). At each indentation increment we solve the following quasi-static weak problem in order to find the displacement field \boldsymbol{u} .

$$\int_{\Omega} P_{iJ} \delta u_{i,J} \, dV = \int_{\partial \Omega_{\text{top}}} fJ G_{KJ} \delta u_{j} \, dA_{I} \,. \tag{30}$$

In Eq. (30), $J = \det(F)$, $G = F^{-1}$, and f(x) is the pressure applied by the indenter normal to the deformed surface. By applying penalty method, the normal contact pressure is computed as $f(x) = P_n H^*(d(x))$, where d(x) is the signed distance of x from its closest point on the indenter, H^* is a smooth Heaviside step function, and P_n is the penalty factor which is set to 0.3E/h, where h is the average mesh element size of sample top boundary and equal to $1.5 \mu m$ in the current model. Scale factor 0.3 is selected based on both ease of convergence and solution accuracy. The lower penalty factor usually leads to faster convergence but more inter-penetration

between contact surfaces. The non linear weak form (30) is solved at each indenter increment for fixed F^p from the previous step. Once the solution u is found, the initial boundary value problem (IBVP) governing the time evolution of each dislocation density is solved. The weak problem corresponding to (13) is

$$\int_{\Omega} (\dot{\varphi}^r \hat{\varphi}^r - \varphi^r w_K^r \hat{\varphi}_{,K}^r) \, dV + \int_{\partial \Omega_{\text{out}}} \varphi^r w_K^r \hat{\varphi}^r \, dA_K = \int_{\Omega} p^r \hat{\varphi}^r \, dV$$
(31)

here $w_K^r = G_{K\beta}^p \tilde{w}^r \tilde{s}_\beta^r$ is the dislocation velocity in the reference configuration, and $\hat{\varsigma}^r$ is the test function. Note that (31) subsumes the condition of zero dislocation flux on the inflow portion of the boundary, hence the boundary term extends only on the outflow boundary $\hat{\sigma}\Omega_{\text{out}}$, defined by the condition $w_K N_N > 0$. The convective term $\hat{\varsigma}_{K}^r w_K^r \hat{\varsigma}^r$ is stabilized by means of the Taylor-Galerkin method (Kuzmin, 2010), where the test function $\hat{\varsigma}^r$ is replaced by $\hat{\varsigma}_{TG}^r = \hat{\varsigma}^r + (\Delta t/2) w_K^r \hat{\varsigma}_{K}^r$, where Δt is the time step. Zero dislocation flux is prescribed on the in-flow portion of the boundary. Together with each ς^r , we also evolve the plastic deformation by solving the spatially-dependent initial value problem (IVP) (9) together with (12). The corresponding weak form is

$$\int_{\Omega} \dot{F}_{\gamma J}^{P} \hat{F}_{\gamma J}^{P} \, \mathrm{d}V = \int_{\Omega} \sum_{r} \tilde{b} \tilde{g}^{r} \tilde{w}^{r} \tilde{s}_{\gamma}^{r} \tilde{n}_{\delta}^{r} F_{\delta J}^{P} \hat{F}_{\gamma J}^{P} \, \mathrm{d}V \tag{32}$$

Eqs. (31) and (32) are used to update the fields g^r and F^P . Since the displacement u is kept fixed during the evolution of F^P , the resolved Mandel stress decreases and dislocation motion eventually stops. When the average absolute value of resolved shear stress over the simulation domain $|\tau^r|_{ave}$ goes down to a stress threshold $\tau_c = 1.1 \mu b/L_2$ indicating most of the dislocations are immobilized, a new indentation step is taken and the overall process repeats until a total indentation depth of $100 \mu m$ is reached. At that point, the motion of the indenter is reversed to unload the sample, and reverse steps are taken until the total load on the indenter vanishes. All material properties are listed in Fig. 2c. The weak forms (30), (31), and (32) have been implemented using the basic PDE module of the commercial FEM software COMSOL multiphysics 5.2.

3.2. Simulation results

As a first comparison between the experimental results of Kysar et al. (2010b) and our model can be made by considering the plot force vs indentation depth shown in Fig. 3. In the range of indentation depth considered here, up to $100\mu m$, there is good agreement between simulations and experiments. Both curves show an initial non-linear relationship between force and depth, which extends to a depth of about $20\mu m$. This initial portion of the loading curve is most likely due to the round tip of the indenter, which has a radius $R = 10\mu m$ in our simulations. Once the lateral sides of the wedge make contact with the material, the load vs depth curve approaches a linear dependence, which is evident in the experimental curve above $d = 70\mu m$. Upon unloading, the elastic recovery of the material is about 10% of the maximum depth in both simulations and experiments.

The total material rotation θ is computed using the polar decomposition of the deformation tensor as F = RU, where R is the orthogonal matrix of rotation. For the two dimensional case considered here, the total material rotation angle θ about the out-of-plane axis can be obtained from the relation $2\cos\theta = \text{tr}(R)$. The simulate material rotation θ is shown in Fig. 4a. Note that the range of the rotation angle θ is determined by the wedge indenter angle. The material in contact with the flanks of the indenter is forced to rotate by an angle equal to half of the wedge angle, that is 45° , while the material under the indenter tip are constrained not to rotate by symmetry considerations. This imposed rotation field is accommodated partially by elastic lattice rotation, and partially by plastic rotation. The angle of rotation of the lattice about the out-of-plane direction, ω_3 , is computed using the polar decomposition of the elastic deformation tensor as $F^E = R^E U^E$, where R^E is the orthogonal matrix of lattice rotation. For the two dimensional case considered here, the lattice rotation angle θ about can be obtained from the relation $2\cos\omega_3 = \text{tr}(R^E)$. Fig. 4b shows the lattice rotation angle in the unloaded state, while Fig. 4c is the corresponding result obtained experimentally by Kysar et al. (2010b). It can be

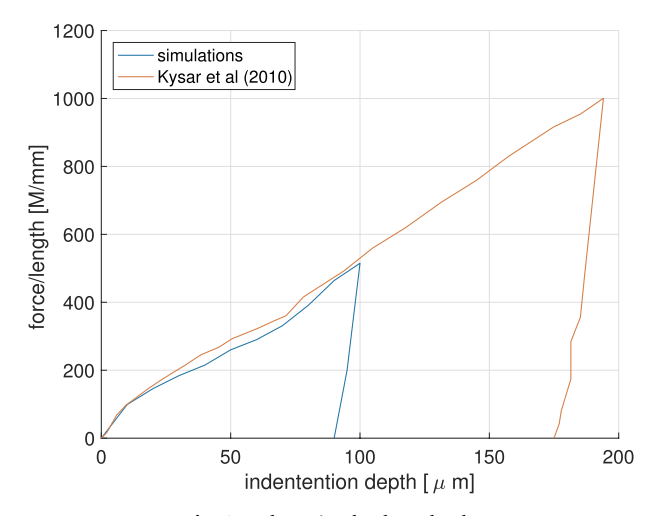


Fig. 3. Indentation load vs. depth.

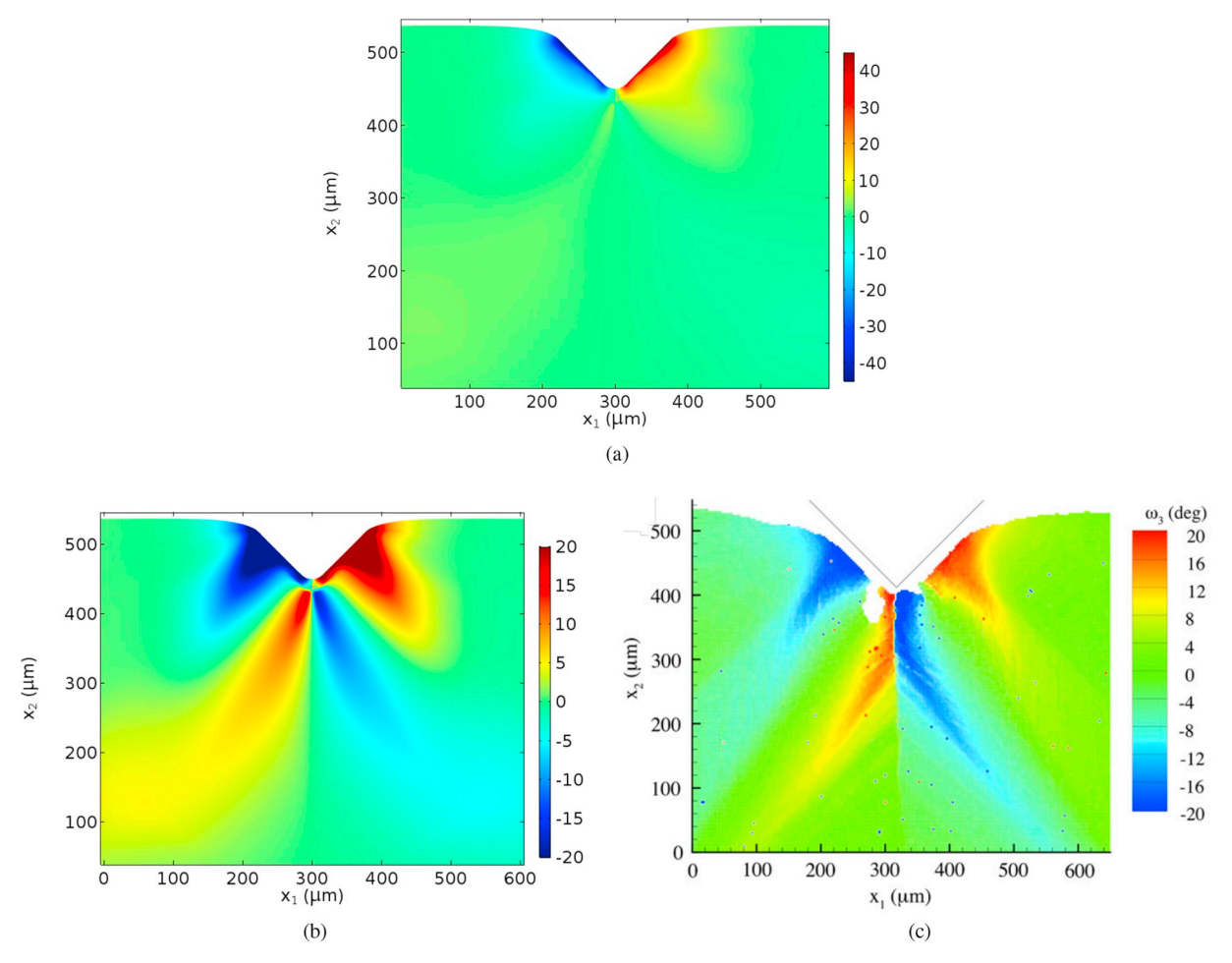


Fig. 4. (a) Total rotation θ computed from our model. (a) Lattice rotation ω_3 computed from our model. (b) Corresponding lattice rotation measured by Kysar et al. (2010b).

observed that the lattice rotation underneath the indenter exhibits four sectors of alternating sign, as predicted by the theory of Hill et al. (1947). The most evident discrepancy between simulation and experimental results can be observed along the vertical line below the indenter tip, where simulations show a diffuse transition between positive and negative rotation sector, whereas experimental results show a sharper transition. The quantitative and qualitative agreement between theory and experiments is remarkable, given the few assumptions made in constructing the current model.

Fig. 5a and c shows the components A_{13} and A_{23} computed from Eq. (6), respectively. The black lines superimposed to these figures represent deformed lattice planes, and they are constructed as being locally tangent to the vector fields $F^c\tilde{e}_1$ and $F^c\tilde{e}_2$, where \tilde{e}_1 and \tilde{e}_2 are the horizontal and vertical unit vectors in the intermediate configuration. Fig. 5a shows a concentration of positive Burgers vector density in the \tilde{e}_1 direction on the vertical line under the indenter, and on two lateral lines that originate approximately at the points of contact of the wedge indenter with the top surface of the crystal. Note that α_{13} represents a density of dislocations with Burgers vector along x_1 . There are five regions of alternating high and low α_{13} intensity, separating the four sectors of lattice rotation. The high Burgers vector density in these regions act as a sort of sub-grain boundary which accommodates the high lattice rotation imposed by the wedge in these regions. Similarly, α_{13} represents a density of dislocations with Burgers vector along x_2 . Their antisymmetric distribution about the mid-plane is best understood by the vertical distorted lattice planes in 5c, which rotate in opposite direction to accommodate the deformation of the indenter.

Fig. 5b and d shows the corresponding components of α_{13} and α_{23} obtained by Kysar et al. (2010b) by post-processing the lattice rotation via Nye's equation

$$\alpha_{ij} = \varepsilon_{jkm} \omega_{ik,m}^e$$
 (33)

Note that (33) uses linearized kinematics and it neglects the contribution of elastic strain. Despite the fact that the experimental results show sharper regions of high density, it can be observed that the general pattern is well reproduced for both fields α_{13} and α_{23} . Next, we consider the distribution of scalar densities on each slip system. In experiments, the problem of reconstructing the densities ϱ^r given α amounts to solving the equation

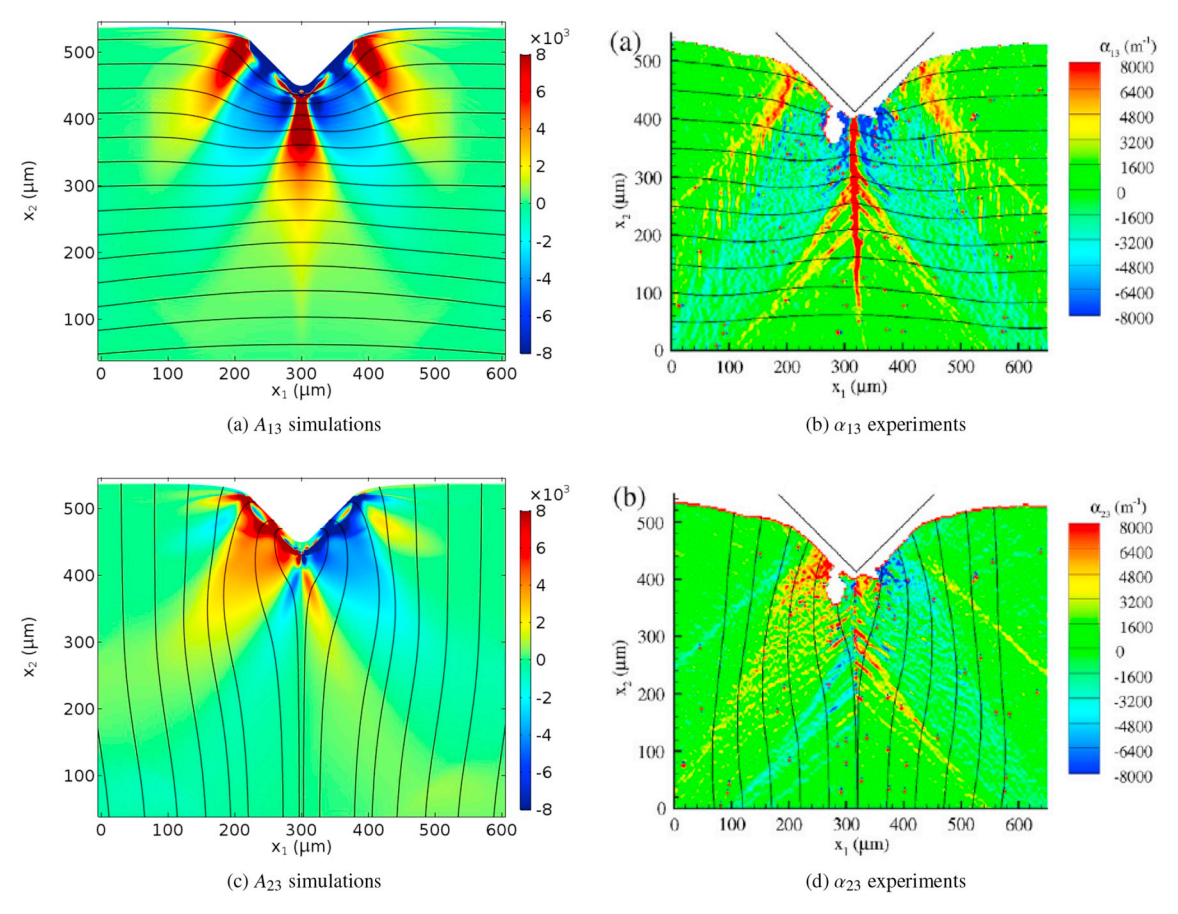


Fig. 5. Comparison between simulated and experimentally-determined sompoen (a) Component of the tensor A_{13} obtained from the simulations. (b) Component of the tensor α_{13} measured experimentally. (a) Component of the tensor A_{23} obtained from the simulations. (d) Component of the tensor α_{23} measured experimentally.

$$\sum_{r} g^{r} \begin{bmatrix} b_{x}^{r} \\ b_{y}^{r} \end{bmatrix} = \begin{bmatrix} \alpha_{13} \\ \alpha_{23} \end{bmatrix}, \tag{34}$$

which is underdetermined for more than two families of dislocations. Kysar et al. (2010b) have eliminated this under-determinacy by requiring that the net dislocation density on each slip system minimizes the L^1 -norm defined as $L^1 = \sum_{\alpha} |\varphi^{\alpha}|_{\text{gnd}} b^{\alpha}$. Results of these calculations were interpreted by Kysar as a "lower bound" estimate of the actual dislocation population, and they are reported in the first column of Fig. 6. The second column of Fig. 6 shows the result of the same calculation using the results of our simulations. It can be observed that for all densities there is very good agreement between corresponding results.

4. Discussion and conclusions

Instrumented indentation has become an ubiquitous tool to investigate the fundamental properties of plasticity at the micro- and nano-scale. In recent years, high-resolution EBSD characterization of these structures has been instrumental in revealing the way materials respond to loads by developing dislocation structures which to accommodate the large deformation induced by indenters. The objective of this paper was to develop a finite-deformation model of indentation that can reproduce the dislocation micro-structure measured in the wedge micro-indentation experiment of Kysar et al. (2010b).

The model presented here has a minimal number of assumptions regarding dislocation generation, multiplication, cross-slip, and junction formation. Nevertheless, it remarkably reproduces essential features of the indentation experiments of Kysar et al. (2010b). The main reason for such agreement may lie in the geometric nature of the experiments and the way they were designed to reveal the GND content of dislocations rather than all dislocation features. First, the experimentally-observed force-displacement curve is quantitatively reproduced with the current model. At very small loads, the response is non-linear, and is found to be determined by the radius of curvature of the indenter's tip. At greater loads, the response is more or less linear over the entire range of loads. Second, it is found that as the hard indenter is pushed into the surface, the material closest to the tip rotates to accommodate adjacent surface rotation, and such immediate material rotation is reversed on a length scale determined by the contact line between the indenter and the surface. Immediate surface rotations become diffuse as a result of dislocation motion a distance of about three times the

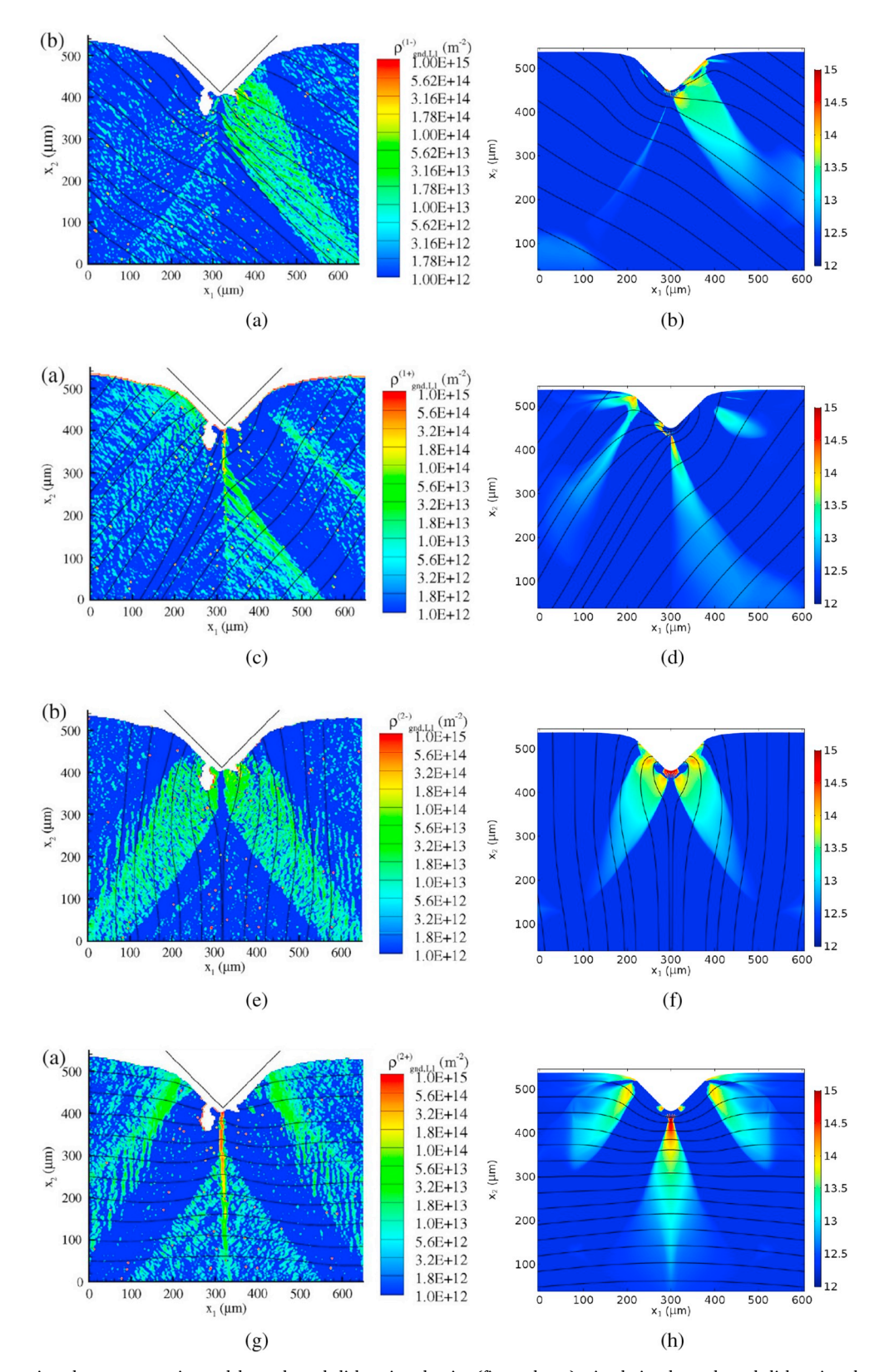


Fig. 6. Comparison between experimental lower-bound dislocation density (first column), simulation lower-bound dislocation density (second column), and actual simulated density (third column), for each slip system. (a)–(b) $g^{(1)}$. (c)–(d) $g^{(2)}$. (e)–(f) $g^{(3)}$. (g)–(h) $g^{(4)}$. Densities $g^{(5)}$ and $g^{(6)}$ are not reported for symmetry reasons.

indentation depth. These two aspects of the experiment are very well-reproduced by the model. Some deviation between the model and experiment is observed adjacent to the symmetry line, where the experiment shows more localized and abrupt rotations near that line, while the simulations show gradual changes.

While the experiment can directly measure lattice rotations and hence the components of the dislocation density tensor, our simulations in fact start from the distributions of dislocation densities on the three equivalent slip systems. From there, the dislocation density tensor and lattice rotations are recovered. Therefore, there is no direct way for the experiment to resolve the individual dislocation densities without recourse to an assumption of total GND density minimization. This can assist in converting measured values of the α -tensor to individual dislocation densities, although the procedure is non-unique. Nevertheless, the simulations reproduce dislocation density distributions in agreement with this assumption and compare well with experiments.

The experiments show finer α -tensor (and hence GND density) patterns that merit further investigations. Those patterns, if confirmed by direct TEM observations under the indenter, may be a result of dislocation self-organization due to a competition between reactions (cross-slip, and junction formation) and transport. The patterns appear to have a wavelength of $50-100\,\mu\text{m}$, but need to be confirmed by TEM observations or higher resolution X-ray diffraction methods. Future modeling that incorporates strong dislocation reactions would then shed direct light on the mechanistic origin of such patterns. The present effort was focused on the global aspects of micro-indentation: force-displacement, rotations, and the α -tensor, and hence an answer to this question awaits further investigation. However, it should be emphasized that the experiment of Kysar et al. (2010b) is only two-dimensional in the sense that the external load induces a state of plane-strain deformation, while the internal dislocation configuration is completely three-dimensional (3D). This means that important dislocation mechanisms such as junction formation and cross-slip exceed the scope of the present approach.

Acknowledgements

The authors acknowledge the support of the U.S. Department of Energy, Office of Fusion Energy, through the DOE award number DE-SC0018410, the Air Force Office of Scientific Research, through award number FA9550-16-1-0444, and the National Science Foundation, Division of Civil, Mechanical and Manufacturing Innovation (CMMI), through award number 1563427 with UCLA. G. Po thanks Amit Acharya for inspiring discussion.

Appendix A. Dislocation balance equation in the reference configuration

We consider a family of dislocations having density ϱ per unit referential area normal to their common line direction defined by the unit vector $\boldsymbol{\xi}$. The corresponding vector density $\varrho = \varrho \boldsymbol{\xi}$ has the property that $\varrho \cdot d\boldsymbol{A}$ is the number of dislocations piercing an elementary oriented area element $d\boldsymbol{A}$ in the reference configuration. Let each dislocation in this bundle possess a generic quantity f. We consider the balance equation governing this quantity for an arbitrary material control surface \mathscr{S}_0 bounded by a closed curve \mathscr{C}_0 . The number of dislocations piercing \mathscr{S}_0 changes as a result of dislocations crossing the curve \mathscr{C}_0 , and as new dislocations of the same type are produced. If dislocations move with velocity \boldsymbol{w} , the number of dislocations crossing an elementary portion of the boundary \mathscr{C}_0 per unit time are those contained in an area element $\boldsymbol{w}dt \times d\boldsymbol{L}$. Therefore the equation expressing the balance of the quantity f is:

$$\frac{d}{dt} \int_{\mathscr{D}_0} f \, \varrho_K dA_K = - \oint_{\mathscr{D}_0} f \, \varepsilon_{BCK} \, \varrho_B w_C dL_K + \int_{\mathscr{D}_0} f p \, \xi_K dA_K, \tag{A.1}$$

where p is the production rate of dislocations. Note that if f = 1, then the left hand side of (A.1) is the rate of change in the total number of dislocations crossing \mathcal{S}_0 , while if $f = \tilde{\boldsymbol{b}}^{(s)}$ is the Burgers vector of each dislocation, then the integral represents the total closure failure of the curve \mathcal{C}_0 mapped to the intermediate configuration.

Application of Stokes's theorem to (A.1) and subsequent localization yields

$$\frac{d}{dt}(f\varphi_K) = -\varepsilon_{KLM}(f\varepsilon_{BCM}\,\varphi_B w_C)_L + fp\xi_K. \tag{A.2}$$

If $f = \tilde{\boldsymbol{b}}^{(s)}$ the following balance equation for the tensorial density $\boldsymbol{A}^r = \boldsymbol{b}^r \otimes \boldsymbol{\rho}^r$ is obtained:

$$\dot{A}_{\alpha K}^{\ r} = -\varepsilon_{KLM}(\varepsilon_{BCM} A_{\alpha B}^{\ r} w_C)_L + p_{\alpha K}^{\ r} = 0. \tag{A.3}$$

On the other hand, if f = 1, we obtain the balance equation for the dislocations, which reads

$$\dot{g}_{K} = -\varepsilon_{KLM}(\varepsilon_{BCM} \, g_{R} w_{C})_{L} + p_{K}. \tag{A.4}$$

In the planar case considered in this paper this reduces to:

$$\dot{\mathbf{g}}_{K} = -(\mathbf{g}_{K}\mathbf{w}_{L})_{L} + p_{K}. \tag{A.5}$$

The referential dislocation velocity \mathbf{w} is the pull-backs of the velocity $\tilde{\mathbf{w}}$ in the intermediate configuration, $w_C = G_{C\gamma}^P \tilde{w}_{\gamma} = G_{C\gamma}^P \tilde{w} \tilde{s}_{\gamma}$. Using this observation and dropping the (constant) unit line direction, we finally obtain the scalar density balance law:

$$\dot{\varphi} = -(\varrho \tilde{w}_{\gamma} G_{K\gamma}^{P})_{,K} + p . \tag{A.6}$$

Appendix B. Balance Laws for energy and entropy

Let us consider a closed material curve \mathscr{C}_0 in the (110) plane of Fig. 1b bounding an area \mathscr{A}_0 , and the prismatic volume $\mathscr{C}_0 = \mathscr{A}_0 \times dz$ obtained by "extruding" the area \mathscr{A}_0 along [110] by a length dz. Balance of energy for this material volume reads

$$\frac{d}{dt} \int_{\mathcal{F}_{\hat{0}}} \left(\frac{1}{2} \rho_0 \nu_i \nu_i + \phi \right) dV = \oint_{\partial \mathcal{F}_{\hat{0}}} \left(P_{iK} \nu_i - Q_K \right) dA_K + \int_{\mathcal{F}_{\hat{0}}} \left(b_k \nu_k + h \right) dV \\
- \oint_{\mathcal{E}_{\hat{0}}} \sum_r \varphi^r dz \, \varepsilon_{BCK} \varsigma_B^r w_C^r dL_K + \int_{\mathcal{F}_{\hat{0}}} \sum_r \varphi^r dz \, p^r dA. \tag{B.1}$$

Here v_i is the material velocity, ϕ the internal energy density per unit referential volume, P_{iK} the first Piola stress, Q_K the heat flux, b_k the body force per uni referential volume, and h the heat supply per unit referential volume. The third therm on the right hand side of Eq. (B.1) represents the energy carried into the control volume by the infinite straight edge dislocations of family r crossing its lateral boundary. Here ϕ^r is an energy per unit length of dislocation. Likewise, the last term represents the energy supply due to the production of dislocations of family r within the same volume.

Since all fields are uniform in the out-of-plane direction, then $\int_{\gamma_0^c} (\cdot) dV = dz \int_{\mathcal{N}_0} (\cdot) dA$. Therefore, applying the divergence theorem to the first term on the rhs, and Stokes theorem to the third term, the factor dz can be dropped from all terms. Accounting for balance of linear momentum, the following integral over \mathcal{N}_0 is obtained

$$\int_{\mathscr{A}_0} \left(\dot{\phi} - P_{iK} \nu_{i,K} + Q_{K,K} - h + \sum_r \xi_K \varepsilon_{KLM} (\varphi^r \varepsilon_{BCM} \, \varrho_B^r w_C^r)_{,L} - \sum_r \varphi^r p^r \right) dA = 0.$$
(B.2)

In the planar case, this equation can be further simplified to

$$\int_{\mathscr{A}_0} \left(\dot{\varphi} - P_{iK} \nu_{i,K} + Q_{K,K} - h + \sum_r \left(\varphi^r \, \wp^r w_K^r \right)_{,K} - \sum_r \varphi^r p^r \right) dA = 0. \tag{B.3}$$

A similar balance equation holds for entropy balance

$$\frac{d}{dt} \int_{\gamma_0} \eta \ dV = -\oint_{\partial \gamma_0} \frac{Q_K}{T} dA_K + \int_{\gamma_0} \frac{h}{T} dV - \oint_{\mathscr{C}_0} \sum_r \sigma^r dz \ \varepsilon_{BCK} \varphi_B^r w_C^r dL_K + \int_{\mathscr{A}_0} \sum_r \sigma^r dz \ p^r dA. \tag{B.4}$$

In Eq. (B.4) η is the entropy density of the material per unit mass, γ is the internal entropy production rate due to irreversible processes, and σ^r is the specific entropy per unit length of dislocation. In the planar case considered here, the entropy balance equation becomes

$$\int_{\mathscr{A}_0} \left(\dot{\eta} + \left(\frac{Q_K}{T} \right)_{,K} - \frac{h}{T} - \gamma + \sum_r \left(\sigma^r \varrho^r w_K^r \right)_{,K} - \sum_r \sigma^r p^r \right) dA = 0.$$
(B.5)

References

Acharya, A., 2001. A model of crystal plasticity based on the theory of continuously distributed dislocations. J. Mech. Phys. Solid. 49 (4), 761-784.

Anstis, G., Chantkul, P., Lawn, B., Marshall, D., 1981. Of indentation techniques for measuring fracture toughness: I, direct crack measurements. J Am. Ceram. Soc. 64 (9), 533–538.

Arsenlis, A., Parks, D., Becker, R., Bulatov, V.V., 2004. On the evolution of crystallographic dislocation density in non-homogeneously deforming crystals. J. Mech. Phys. Solid. 52 (6), 1213–1246.

Baitsch, M., Le, K., Tran, T., 2015. Dislocation structure during microindentation. Int. J. Eng. Sci. 94, 195–211.

Balint, D., Deshpande, V., Needleman, A., Van der Giessen, E., 2006. Discrete dislocation plasticity analysis of the wedge indentation of films. J. Mech. Phys. Solid. 54 (11), 2281–2303.

Berdichevsky, V.L., 2006. Continuum theory of dislocations revisited. Continuum Mech. Therm. 18, 195-222.

Bilby, B.A., Gardner, L., Stroh, A.N., 1957. Continuous distributions of dislocations and the theory of plasticity. In: Proceedings of the Ninth International Congress on Applied Mechanics, Bruxelles, pp. 35–44.

Bitzek, E., Gumbsch, P., 2005. Dynamic aspects of dislocation motion: atomistic simulations. Mater. Sci. Eng., A 400, 40-44.

Cermelli, P., Gurtin, M.E., 2001. On the characterization of geometrically necessary dislocations in finite plasticity. J. Mech. Phys. Solid. 49 (7), 1539-1568.

Cheng, Y.T., Cheng, C.M., 2004. Scaling, dimensional analysis, and indentation measurements. Mater. Sci. Eng. R Rep. 44 (4-5), 91-150.

Collins, I., Houlsby, G., 1997. Application of thermomechanical principles to the modelling of geotechnical materials. Proc. Roy. Soc. Lond. Mater. 453, 1975–2001. Dahlberg, C., Saito, Y., Öztop, M.S., Kysar, J.W., 2014. Geometrically necessary dislocation density measurements associated with different angles of indentations. Int. J. Plast. 54, 81–95.

de la Fuente, O.R., Zimmerman, J., Gonzalez, M., De la Figuera, J., Hamilton, J., Pai, W.W., Rojo, J., 2002. Dislocation emission around nanoindentations on a (001) fcc metal surface studied by scanning tunneling microscopy and atomistic simulations. Phys. Rev. Lett. 88 (3), 036101.

de Wit, R., 1960. The continuum theory of stationary dislocations. Solid State Phys. 10, 249-292.

de Wit, R., 1965. The direction of the force on a dislocation and the sign of the Burgers vector. Acta Metall. 1210-1211.

Demir, E., Raabe, D., Zaafarani, N., Zaefferer, S., 2009. Investigation of the indentation size effect through the measurement of the geometrically necessary dislocations beneath small indents of different depths using ebsd tomography. Acta Mater. 57 (2), 559–569.

Engels, P., Ma, A., Hartmaier, A., 2012. Continuum simulation of the evolution of dislocation densities during nanoindentation. Int. J. Plast. 38, 159-169.

Fang, T.-H., Weng, C.-I., Chang, J.-G., 2003. Molecular dynamics analysis of temperature effects on nanoindentation measurement. Mater. Sci. Eng., A 357 (1–2), 7–12. Fischer-Cripps, A.C., 2006. Critical review of analysis and interpretation of nanoindentation test data. Surf. Coating. Technol. 200 (14–15), 4153–4165.

Fivel, M., Robertson, C., Canova, G., Boulanger, L., 1998. Three-dimensional modeling of indent-induced plastic zone at a mesoscale1. Acta Mater. 46 (17), 6183-6194

Fivel, M., Verdier, M., Canova, G., 1997. 3d simulation of a nanoindentation test at a mesoscopic scale. Mater. Sci. Eng., A 234, 923-926.

Gan. Y., Chen. X., Zhao, M., 2008. Numerical and experimental studies of deep indentation on single crystals, J. Mech. Mater. Struct. 3 (8), 1429–1445.

Gouldstone, A., Chollacoop, N., Dao, M., Li, J., Minor, A.M., Shen, Y.-L., 2007. Indentation across size scales and disciplines: recent developments in experimentation and modeling. Acta Mater. 55 (12), 4015–4039.

Groma, I., Györgyi, G., Ispánovity, P.D., 2010. Variational approach in dislocation theory. Phil. Mag. 90 (27-28), 3679-3695.

Groma, I., Györgyi, G., Kocsis, B., 2007. Dynamics of coarse grained dislocation densities from an effective free energy. Phil. Mag. 87 (8-9), 1185-1199.

Hannink, R.H.J., Kohlstedt, D.L., Murray, M.J., 1972. Slip system determination in cubic carbides by hardness anisotropy. Proc. Math. Phys. Eng. Sci. 326, 409–420. Hill, R., Lee, E., Tupper, S., 1947. The theory of wedge indentation of ductile materials. In: Proc. R. Soc. Lond. A. vol. 188. The Royal Society, pp. 273–289.

Hochrainer, T., Sandfeld, S., Zaiser, M., Gumbsch, P., 2014. Continuum dislocation dynamics: towards a physical theory of crystal plasticity. J. Mech. Phys. Solid. 63, 167–178

Kooiman, M., Hütter, M., Geers, M., 2014. Collective behaviour of dislocations in a finite medium. J. Stat. Mech. Theor. Exp. 2014 (4), P04028.

Kooiman, M., Hütter, M., Geers, M., 2015. Microscopically derived free energy of dislocations. J. Mech. Phys. Solid. 78, 186-209.

Kooiman, M., Hütter, M., Geers, M., 2016. Free energy of dislocations in a multi-slip geometry. J. Mech. Phys. Solid. 88, 267-273.

Kröner, E., 1960. Allgemeine Kontinuumstheorie der Versetzungen Und Eigenspannungen. Arch. Ration. Mech. Anal. 4 (4), 273-334.

Kuzmin, D., 2010. A Guide to Numerical Methods for Transport Equations.

Kysar, J., Saito, Y., Oztop, M., Lee, D., Huh, W., 2010a. Experimental lower bounds on geometrically necessary dislocation density. Int. J. Plast. 26 (8), 1097–1123. Kysar, J.W., Gan, Y.X., Mendez-Arzuza, G., 2005. Cylindrical void in a rigid-ideally plastic single crystal. part i: anisotropic slip line theory solution for face-centered cubic crystals. Int. J. Plast. 21 (8), 1481–1520.

Kysar, J.W., Gan, Y.X., Morse, T.L., Chen, X., Jones, M.E., 2007. High strain gradient plasticity associated with wedge indentation into face-centered cubic single crystals: geometrically necessary dislocation densities. J. Mech. Phys. Solid. 55 (7), 1554–1573.

Kysar, J.W., Saito, Y., Oztop, M.S., Lee, D., Huh, W.T., 2010b. Experimental lower bounds on geometrically necessary dislocation density. Int. J. Plast. 26 (8), 1097–1123.

Lee, E., 1969. Elastic-plastic deformation at finite strains. J. Appl. Mech. 36 (1), 1-6.

Lee, W., Chen, Y., 2010. Simulation of micro-indentation hardness of fcc single crystals by mechanism-based strain gradient crystal plasticity. Int. J. Plast. 26 (10), 1527–1540.

Li, J., Van Vliet, K.J., Zhu, T., Yip, S., Suresh, S., 2002. Atomistic mechanisms governing elastic limit and incipient plasticity in crystals. Nature 418 (6895), 307.

Li, X., Bhushan, B., 2002. A review of nanoindentation continuous stiffness measurement technique and its applications. Mater. Char. 48 (1), 11-36.

Li, X., Diao, D., Bhushan, B., 1997. Fracture mechanisms of thin amorphous carbon films in nanoindentation. Acta Mater. 45 (11), 4453-4461.

Lilleodden, E., Zimmerman, J., Foiles, S., Nix, W., 2003. Atomistic simulations of elastic deformation and dislocation nucleation during nanoindentation. J. Mech. Phys. Solid. 51 (5), 901–920.

Lothe, J., 1962. Theory of dislocation mobility in pure slip. J. Appl. Phys. 33 (6), 2116-2125.

Malvern, L.E., 1969. Introduction to the Mechanics of a Continuous Medium. Number Monograph.

Mesarovic, S.D., Baskaran, R., Panchenko, A., 2010. Thermodynamic coarsening of dislocation mechanics and the size-dependent continuum crystal plasticity. J. Mech. Phys. Solid. 58 (3), 311–329.

Mura, T., 1982. Micromechanics of Defects in Solids.

Nabarro, F.R., 1967. Theory of Crystal Dislocations.

Nair, A.K., Parker, E., Gaudreau, P., Farkas, D., Kriz, R.D., 2008. Size effects in indentation response of thin films at the nanoscale: a molecular dynamics study. Int. J. Plast. 24 (11), 2016–2031.

Nix, W.D., Gao, H.J., 1998. Indentation size effects in crystalline materials: a law for strain gradient plasticity. J. Mech. Phys. Solid. 46 (3), 411-425.

Nye, J., 1953. Some geometrical relations in dislocated crystals. Acta Metall. Mater. 1 (2), 153-162.

Oliver, W.C., Pharr, G.M., 1992. An improved technique for determining hardness and elastic modulus using load and displacement sensing indentation experiments. J. Mater. Res. 7 (6), 1564–1583.

Olmsted, D.L., Hector Jr., L.G., Curtin, W., Clifton, R., 2005. Atomistic simulations of dislocation mobility in al, ni and al/mg alloys. Model. Simulat. Mater. Sci. Eng. 13 (3), 371.

Owen, E., Yates, E., Sully, A., 1937. An x-ray investigation of pure iron-nickel alloys. part 4: the variation of lattice-parameter with composition. Proc. Phys. Soc. 49 (3), 315.

Öztop, M.S., Niordson, C.F., Kysar, J.W., 2013. Length-scale effect due to periodic variation of geometrically necessary dislocation densities. Int. J. Plast. 41, 189–201. Pethicai, J.B., Hutchings, R., Oliver, W.C., 1983. Hardness measurement at penetration depths as small as 20 nm. Philos. Mag. A: Phys. Conden. Matter Struct., Defect. Mech. Proper. 48 (4), 593–606.

Pharr, G.M., Herbert, E.G., Gao, Y., 2010. The indentation size effect: a critical examination of experimental observations and mechanistic interpretations. Annu. Rev. Mater. Res. 40 (1), 271–292.

Po, G., Ghoniem, N., 2012. Modeling of dislocation microstructure evolution in microindentation experiments. In: Khan, Akhtar S. (Ed.), Proc. Of the 18th International Symposium on Plasticity and its Current Applications, San Juan, PR, January 3-8, 2012. The Royal Society.

Po, G., Mohamed, M.S., Crosby, T., Erel, C., El-Azab, A., Ghoniem, N., 2014. Recent progress in discrete dislocation dynamics and its applications to micro plasticity. JOM (J. Occup. Med.) 66 (10), 2108–2120.

Rester, M., Motz, C., Pippan, R., 2008. Stacking fault energy and indentation size effect: do they interact? Scripta Mater. 58 (3), 187-190.

Reuber, C., Eisenlohr, P., Roters, F., Raabe, D., 2014. Dislocation density distribution around an indent in single-crystalline nickel: comparing nonlocal crystal plasticity finite-element predictions with experiments. Acta Mater. 71, 333–348.

Roters, F., Eisenlohr, P., Hantcherli, L., Tjahjanto, D.D., Bieler, T.R., Raabe, D., 2010. Overview of constitutive laws, kinematics, homogenization and multiscale methods in crystal plasticity finite-element modeling: theory, experiments, applications. Acta Mater. 58 (4), 1152–1211.

Ruggles, T., Fullwood, D., Kysar, J., 2016. Resolving geometrically necessary dislocation density onto individual dislocation types using ebsd-based continuum dislocation microscopy. Int. J. Plast. 76, 231–243.

Sabnis, P.A., Forest, S., Arakere, N.K., Yastrebov, V.A., 2013. Crystal plasticity analysis of cylindrical indentation on a ni-base single crystal superalloy. Int. J. Plast. 51, 200–217.

Saito, Y., Oztop, M.S., Kysar, J.W., 2012. Wedge indentation into elastic-plastic single crystals. 2: simulations for face-centered cubic crystals. Int. J. Plast. 28 (1), 70–87.

Schuh, C.A., 2006. Nanoindentation studies of materials. Mater. Today 9 (5), 32-40.

Schwaiger, R., Kraft, O., 1999. High cycle fatigue of thin silver films investigated by dynamic microbeam deflection. Scripta Mater. 41 (8), 823–829.

Steinmann, P., 1996. Views on multiplicative elastoplasticity and the continuum theory of dislocations. Int. J. Eng. Sci. 34 (15), 1717–1735.

Suresh, S., Giannakopoulos, A., 1998. A new method for estimating residual stresses by instrumented sharp indentation. Acta Mater. 46 (16), 5755-5767.

Svendsen, B., 2002. Continuum thermodynamic models for crystal plasticity including the effects of geometrically-necessary dislocations. J. Mech. Phys. Solid. 50 (6), 1297–1329.

Svendsen, B., Bargmann, S., 2010. On the continuum thermodynamic rate variational formulation of models for extended crystal plasticity at large deformation. J. Mech. Phys. Solid. 58 (9), 1253–1271.

Tabor, D., 1951. The Hardness of Metals. Clarendon Press, Oxford.

Teodosiu, C., 1982. Elastic Models of Crystal Defects. Springer Science & Business Media.

Vanlandingham, M.R., 2003. Rev. Instrum. Inden. 108 (4), 249-265.

Xia, S., El-Azab, A., 2015. Computational modelling of mesoscale dislocation patterning and plastic deformation of single crystals. Model. Simulat. Mater. Sci. Eng. 23 (5), 055009.

Xiong, L., Deng, Q., Tucker, G.J., McDowell, D.L., Chen, Y., 2012. Coarse-grained atomistic simulations of dislocations in al, ni and cu crystals. Int. J. Plast. 38, 86–101. Xue, Z., Huang, Y., Hwang, K., Li, M., 2002. The influence of indenter tip radius on the micro-indentation hardness. J. Eng. Mater. Technol. 124 (3), 371–379. Yefimov, S., Groma, I., Van der Giessen, E., 2004. A comparison of a statistical-mechanics based plasticity model with discrete dislocation plasticity calculations. J.

Mech. Phys. Solid. 52 (2), 279-300.

Zaafarani, N., Raabe, D., Roters, F., Zaefferer, S., 2008. On the origin of deformation-induced rotation patterns below nanoindents. Acta Mater. 56 (1), 31–42. Zaafarani, N., Raabe, D., Singh, R., Roters, F., Zaefferer, S., 2006. Three-dimensional investigation of the texture and microstructure below a nanoindent in a cu single crystal using 3d ebsd and crystal plasticity finite element simulations. Acta Mater. 54 (7), 1863–1876.

Zhang, F., Saha, R., Huang, Y., Nix, W., Hwang, K., Qu, S., Li, M., 2007. Indentation of a hard film on a soft substrate: strain gradient hardening effects. Int. J. Plast. 23 (1), 25–43.

Zhang, Y., Gao, Y., Nicola, L., 2014. Lattice rotation caused by wedge indentation of a single crystal: dislocation dynamics compared to crystal plasticity simulations. J. Mech. Phys. Solid. 68, 267–279.

Ziegler, H., 1983. An Introduction to Thermomechanics (North-Holland Series in Applied Mathematics and Mechanics), 2 Rev Sub ed. Elsevier Science Ltd. Ziegler, H., Wehrli, C., 1987. The derivation of constitutive relations from the free energy and the dissipation function. Adv. Appl. Mech. 25, 183–238.